International Journal of Thermophysics, Vol. 28, No. 1, February 2007 (© 2007)
DOI: 10.1007/s10765-007-0160-8

Density and Thermal Conductivity Measurements for Silicon Melt by Electromagnetic Levitation under a Static Magnetic Field

Y. Inatomi,[1,2,3] F. Onishi,[2] K. Nagashio,[1] and K. Kuribayashi[1]

Received: June 16, 2006

The density and thermal conductivity of a high-purity silicon melt were measured over a wide temperature range including the undercooled regime by non-contact techniques accompanied with electromagnetic levitation (EML) under a homogeneous and static magnetic field. The maximum undercooling of 320 K for silicon was controlled by the residual impurity in the specimen, not by the melt motion or by contamination of the material. The temperature dependence of the measured density showed a linear relation for temperature as: $\rho(T) = 2.51 \times 10^3 - 0.271(T - T_m)\,\mathrm{kg \cdot m^{-3}}$ for $1367\,\mathrm{K} < T < 1767\,\mathrm{K}$, where T_m is the melting point of silicon. A periodic heating method with a CO_2 laser was adopted for the thermal conductivity measurement of the silicon melt. The measured thermal conductivity of the melt agreed roughly with values estimated by a Wiedemann–Franz law.

KEY WORDS: density; electromagnetic levitation; non-contact measurement; numerical simulation; silicon melt; static magnetic field; thermal conductivity; undercooling.

1. INTRODUCTION

Containerless processing by a levitation method has been used for materials science and technological applications such as rapid solidification, purification, and thermophysical properties measurement of melts [1,2]. Most materials can be cooled even below their melting points and remain in

[1]Institute of Space and Astronautical Science, Japan Aerospace Exploration Agency, 3-3-1 Yoshinodai, Sagamihara, Kanagawa 229-8510, Japan.
[2]School of Physical Sciences, The Graduate University for Advanced Studies, 3-3-1 Yoshinodai, Sagamihara, Kanagawa 229-8510, Japan.
[3]To whom correspondence should be addressed. E-mail: inatomi@isas.jaxa.jp

a liquid state if the melt is not contaminated and undisturbed by the atmosphere. Deep undercooling makes it possible to create a non-equilibrium phase in a melt and to reveal a structural change of the melt. Thermophysical properties of melts are obviously sensitive to contamination. Contact with the container provides contamination to the melt, and it can also alter the measurements.

There are several techniques for containerless processing: gas-jet levitation [3], magnetic levitation [4, 5], electrostatic levitation [6, 7], and electromagnetic levitation (EML) [8, 9]. For gas-jet levitation the gravitational force is balanced by the aerodynamic force of gas flow from the nozzle. Although a gas-jet can levitate non-electrically conductive materials, it is hard to adjust gas flow taking into account the surface tension of the specimen. For the case of magnetic levitation, the gravitational force is compensated at the level of individual atoms and molecules, while a magnet generating a large magnetic force is required to levitate a metallic melt. Electrostatic levitation can make a charged specimen to levitate in vacuum by the electrostatic force. The electrical conductivity of the specimen does not influence the levitation force, but the levitated specimen is smaller than those for other levitation methods and the specimen is usually processed in vacuum to prevent arcing. EML can be used to levitate a relatively large size of a metallic melt in a given atmosphere. However, turbulent convection and vibration are usually observed on the melt surface. Since both heating and levitation of the specimen are simultaneously achieved by an electromagnetic field generated by a radio-frequency (RF) coil, independent control for the temperature and spatial position of the specimen is difficult and the strong Lorentz force yields electromagnetic stirring in the melt and destabilizes the shape of the melt. In addition, blowing of gas to the levitated melt potentially induces spontaneous nucleation due to vibration, and thus the vibration as well as the deformation of the melt must be damped.

Levitation of specimens on earth can produce questionable results due to flow within the specimen. Going to space, where most effects from the gravitational force can be eliminated, is expected to be the best way to solve the problem. Recently, the application of a static magnetic field to an electrically conducting melt has been recognized as a method to substitute for a low-gravity environment [10, 11], because the motion of the melt is reduced by interaction between the imposed static magnetic field and the electric current induced by the field [12]. There have been several reports concerning a cold crucible induction furnace setup fitting in the bore of a magnet [13, 14]. Yasuda et al. developed a novel method for levitating a metallic melt by EML under a static magnetic field in order to damp the convection and vibration in the melt by the Lorentz force

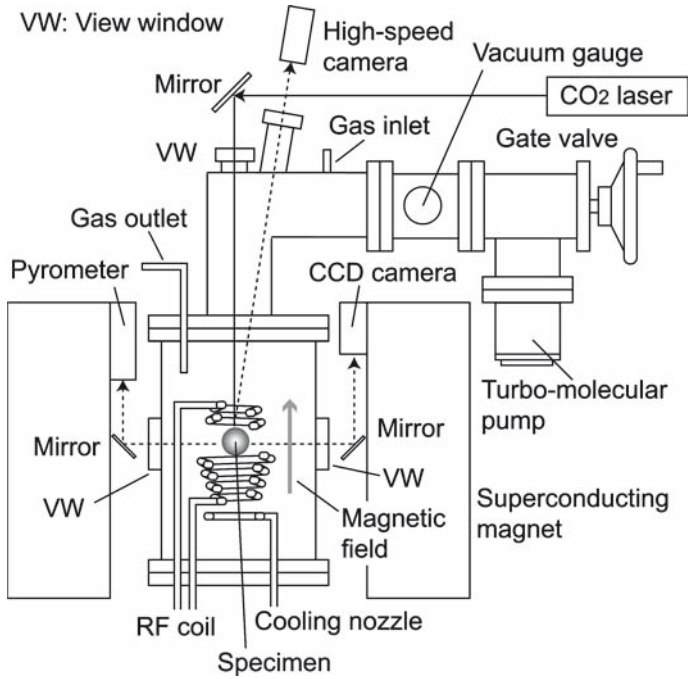

Fig. 1. Schematic diagram of experimental setup.

induced by the magnetic field [15, 16]. In the present study, the density and thermal conductivity of a high-purity silicon melt were measured by EML under a homogeneous and static magnetic field. Silicon is important from an industrial view point as well as a subject of fundamental research. The determination of the thermophysical properties of silicon melt is essential in numerical calculations for crystal growth processes.

2. EXPERIMENTAL

2.1. Experimental Setup

Figure 1 shows a schematic diagram of an experimental setup for measurements of the thermophysical properties of a levitated melt under a static magnetic field. An RF generator with a frequency of 200 kHz and a maximum power of 15 kW was connected to an RF levitation coil. A specimen was placed on a specimen holder made of boron nitride and was transferred to the bottom of the RF coil. A vacuum chamber for levitation was evacuated to 10^{-6} Pa with a turbo-molecular pump and then

filled with argon gas of 99.999% purity. VCR fittings were used for joints between stainless pipes and the chamber. The degree of vacuum in the chamber was held at less than 10^{-2} Pa after 1 h without additional evacuation. A homogeneous and static magnetic field with a maximum magnetic flux density of 6 T was produced by a liquid helium-free superconducting magnet with a bore of 300 mm diameter and 600 mm length (Toshiba, TM-6VH30) [17]. A cube of solid material was preheated on the specimen holder by a 100 W continuous wave CO_2 laser with a wavelength of 10.6 μm (Synrad, Model 57-2) to increase the electrical conductivity of the specimen for levitation. The laser beam was focused down to a spot size of 2 mm by ZnSe lenses and then transmitted to the top of the specimen through a ZnSe view window of the vacuum chamber. The specimen was partially melted by laser irradiation, and was then melted completely and levitated by the induction current generated by the RF coil with constant output power.

The surface temperature at the equator of the levitated melt was measured using a monochromatic optical pyrometer (Japan Sensor, FTZ6, effective wavelength: from 0.8 to 1.6 μm, spot size: 1.7 mm, and sampling rate: 100 Hz) through a side-view window of the vacuum chamber. Reflection of the CO_2 laser irradiation at the specimen surface is invisible for the pyrometer. The specimen temperature was controlled by adjustment of the output power of the RF levitation coil and flow rate of the argon–helium mixed gas through a cooled nozzle for the specimen. Blowing of the gas to the melt was also used to control the atmosphere around the melt. The specimen temperature was calibrated by a blackbody furnace (Tokyo Seiko, BTF-M14) and by a recalescence measurement of a solid–liquid coexistence state in the pure melt. A high-speed camera of 10,000 frames/s (Photron, FASTCAM-PCI) and a 400,000-pixel CCD camera of 30 frames/s were mounted to observe the motion and shape of the melt motion in real time. A telecentric lens system was adopted to create an image that maintained constant size at unknown and varying object distance from the lens system [18].

2.2. Density and Thermal Conductivity Measurements

Non-doped polycrystalline silicon of 99.99999% purity, 0.7 g mass, and 8 mm diameter was used as the specimen. The specimen surface was etched in a mixed aqueous solution of hydrogen fluoride and nitric acid to remove contamination adhered on the surface. Video images of a levitated specimen were obtained by the CCD camera through the side-view window, and were recorded on a digital video recorder after the surface temperature of the melt attained a given temperature. The video images

were stored on a computer through an IEEE 1394 interface and were subsequently converted to sequential image files.

The density of the melt was determined by dividing the initial mass, which was measured before the experiment, by the volume V calculated with an outline of the specimen. Bradshaw et al. [19] employed a noncontact method for ESL to measure the volume of symmetric samples with high precision. However, the captured image in the present measurement was not analyzed using their subpixel edge detection technique due to oscillation and slight asymmetry of the sample levitated by EML. Figure 2 shows a sequence to measure the outline of the melt and to make an axial symmetry model used for a numerical simulation as described in Section 3. The edge of the melt is detected to create an edge line with single pixel resolution by calculating the absolute value of the maximum gradient in the image using an image processing software. The edge line is divided into left and right parts with about the same shape at the z coordinate as the centerline, and then these parts are defined as two functions of z_i, $S_L(z_i)$, and $S_R(z_i)$, where z_i is the point with index $i = 1, 2, 3, \ldots, N$ on the z coordinate and N is the total number of edge points on each line. Since the rotation axis of the asymmetric melt is usually tilted from the axis of the RF coil more or less, the original edge line is rotated at intervals of 0.1 degree steps so that the deviation of $S_L(z_i)$ from $S_R(z_i)$ was minimized, and thus the averaged outline of the melt $S_{Ave} = (S_L + S_R)/2$ is determined. Consequently, the melt volume V is obtained by the following approximation using a finite summation of $S^2_{Ave}(z_i)$ as

$$V = \pi\,(\Delta z)^3 \sum_{i=1}^{N} {S_{Ave}}^2(z_i), \tag{1}$$

where $z_i = i\ \Delta z$, $\Delta z = \Lambda/N$, and Λ is the height of the melt. The above procedure is applied to each sequential image obtained at the same temperature in order to choose the outline with the most left–right symmetry.

A periodic heating method with a CO_2 laser [20,21] was adopted for the thermal conductivity measurement of the silicon melt. Laser irradiation at a sinusoidal modulation frequency of 0.5 Hz, which was controlled by a function generator, was focused on a 2 mm diameter spot at the top surface of the specimen. The CO_2 laser was specified to produce single-mode TEM00 irradiation. Figure 3 shows typical histories of a control signal for the laser power and temperature at the equator of the melt as a response for the modulated irradiation of the laser. The thermal conductivity was determined by obtaining the phase delay of the surface temperature oscillation $\Delta\varphi$ at the equator of the melt from the output oscillation of the laser power.

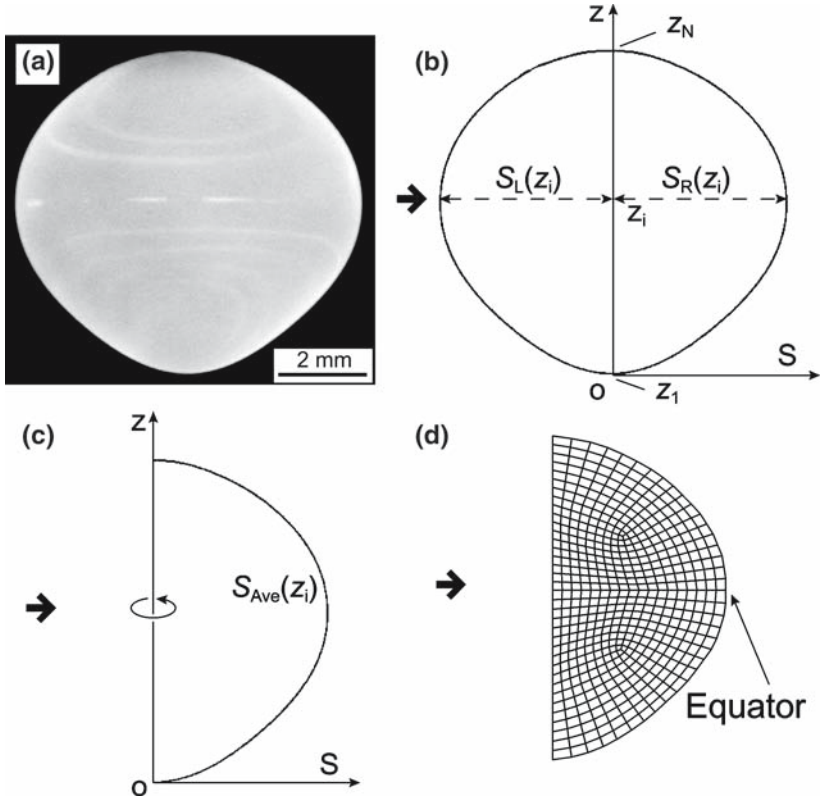

Fig. 2. Sequence to measure outline of silicon melt and to make axial symmetry model used for a numerical simulation: (a) photo of levitated silicon melt, (b) outlines of the melt $S_L(z)$ and $S_R(z)$, (c) averaged outline of the melt S_{Ave}, and (d) element mesh for the melt.

3. ANALYSIS OF PERIODIC HEATING METHOD FOR SPECIMEN

In this research it was assumed that heat transport in a spherical specimen was conductive. A phase delay $\Delta\varphi$ defined in the periodic heating method is derived by accounting for the heat exchange between the melt and the atmosphere. A governing equation, a boundary condition, and an initial condition for axi-symmetric heat conduction in a sphere are expressed in the spherical coordinate system according to the following equations, where the variables are defined as: ρ, density; t, time; C_P, specific heat; k, thermal conductivity; r, radius; T, temperature: T_{ref}, reference temperature; ε, total hemispherical emissivity; σ_B, Boltzmann constant;

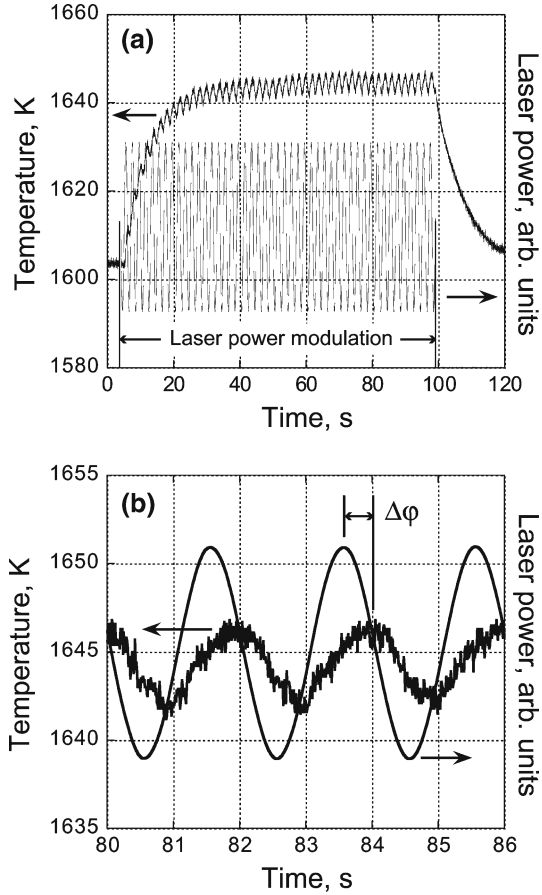

Fig. 3. Temperature history at the equator of the melt as a response for modulated irradiation of CO_2 laser: (a) typical histories of control signal for laser power and temperature, and (b) phase delay of the temperature from the sinusoidal laser power.

H, calorific power per unit time and unit volume; and $h_g(\theta)$, local heat transfer coefficient.

Heat transport equation

$$\rho C_P \frac{\partial T}{\partial t} = k \left\{ \frac{1}{r^2} \frac{\partial}{\partial r} \left(r^2 \frac{\partial T}{\partial r} \right) + \frac{1}{r^2 \sin\theta} \frac{\partial}{\partial \theta} \left(\sin\theta \frac{\partial T}{\partial \theta} \right) \right\} + H(r, \theta), \qquad (2)$$

where H is assumed to be time-independent because of constant output power of the RF coil.

Boundary condition at specimen surface

$$k \left.\frac{\partial T}{\partial r}\right|_{r=R} = -\varepsilon\sigma_{\mathrm{B}}\left(T^4 - T_{\mathrm{ref}}^4\right) - h_{\mathrm{g}}(\theta)\,(T - T_{\mathrm{ref}}) + F_0(\theta)\,(Q_0 + Q_1 \sin\omega_0 t)\,. \tag{3}$$

The first, second, and third terms of the right-hand side in Eq. (3) correspond to radiation, convective heat transfer, and applied heat flux, respectively.

Initial condition

$$T(r, \theta, 0) = T_0(r, \theta)\,. \tag{4}$$

Equations (2) and (3) were separated to steady-state and non-steady-state terms by

$$T(r, \theta, t) = T_0(r, \theta) + T_{\mathrm{D}}(r, \theta, t)\,. \tag{5}$$

Only the non-steady-state term in Eq. (5) is solved to derive the phase delay $\Delta\varphi$ as follows:

Heat transport equation

$$\frac{\partial T_{\mathrm{D}}}{\partial t} = \frac{k}{\rho C_P}\left\{\frac{1}{r^2}\frac{\partial}{\partial r}\left(r^2\frac{\partial T_{\mathrm{D}}}{\partial r}\right) + \frac{1}{r^2\sin\theta}\frac{\partial}{\partial\theta}\left(\sin\theta\frac{\partial T_{\mathrm{D}}}{\partial\theta}\right)\right\}. \tag{6}$$

Boundary condition at specimen surface

The second term of the right-hand side in Eq. (3) is approximated linearly about a point $T = T_0$ as

$$k \left.\frac{\partial T_{\mathrm{D}}}{\partial r}\right|_{r=R} = -\left(4\varepsilon\sigma_{\mathrm{B}}T_0^3 + h_{\mathrm{g0}}\right)T_{\mathrm{D}} + F_0(\theta)\,(Q_0 + Q_1\sin\omega_0 t)\,, \tag{7}$$

where h_{g0} is assumed to be an averaged value of $h_{\mathrm{g}}(\theta)$ for θ.

Initial condition

$$T_{\mathrm{D}}(R, \theta, 0) = 0, \tag{8}$$

The temperature on the surface $T_D(R, \theta, t)$ is obtained by solving the partial differential equation, Eq. (6), with Eqs. (7) and (8) based on separation of variables.

$$\begin{aligned} T_{\mathrm{D}}(R, \theta, t) &= \frac{R}{k}\left\{Q_0 E_0(\theta, t) + Q_1 E_1(\theta)\sin\omega_0 t - Q_1 E_2(\theta)\cos\omega_0 t\right\} \\ &= \frac{R}{k}\left\{Q_0 E_0 + Q_1\sqrt{E_1^2 + E_2^2}\sin(\omega_0 t - \Delta\varphi)\right\} \end{aligned} \tag{9a}$$

$$\cos \Delta\varphi = \frac{E_1}{\sqrt{E_1^2 + E_2^2}} \tag{9b}$$

$$E_0(\theta, t) = \sum_{m=0}^{\infty} \sum_{n=0}^{\infty} \left\{ 1 - \left(1 - \frac{Q_1}{Q_0} \frac{\omega a_{m,n}^2}{a_{m,n}^4 + \omega^2} \right) \exp\left(-\frac{a_{m,n}^2}{\omega} \omega_0 t \right) \right\} K_{m,n}(\theta) \tag{9c}$$

$$E_1(\theta) = \sum_{m=0}^{\infty} \sum_{n=0}^{\infty} \frac{a_{m,n}^4}{a_{m,n}^4 + \omega^2} K_{m,n}(\theta) \tag{9d}$$

$$E_2(\theta) = \sum_{m=0}^{\infty} \sum_{n=0}^{\infty} \frac{\omega a_{m,n}^2}{a_{m,n}^4 + \omega^2} K_{m,n}(\theta) \tag{9e}$$

$$K_{m,n}(\theta) = M_{m,n} I_m P_m(\cos\theta) \tag{9f}$$

$$M_{m,n} = \frac{2m+1}{a_{m,n}^2 - m(m+1) - h(1-h)} \tag{9g}$$

$$h = \frac{\left(4\varepsilon\sigma_B T_0^3 + h_{g0}\right) R}{k} \tag{9h}$$

$$\omega = \frac{\rho C_p R^2 \omega_0}{k} \tag{9i}$$

$$I_m = \int_0^{\pi} F_0(\phi) \sin\phi P_m(\cos\phi)\, d\phi \tag{9j}$$

$$a_{m,n} j_m'\left(a_{m,n}\right) + h j_m\left(a_{m,n}\right) = 0 \tag{9k}$$

where j_m(x) and P_m(x) are a spherical Bessel function and a Legendre polynomial of order m, respectively.

Taking into account single-mode TEM00 irradiation by the CO_2 laser, the angle θ dependence of heat flux on the surface by laser irradiation is expressed as follows:

$$F_0(\theta) = \begin{cases} \exp\left(-\frac{2}{A^2}\sin^2\theta\right)\cos\theta; & \text{for } 0 \leqslant \theta \leqslant \frac{\pi}{2} \\ 0; & \text{for } \frac{\pi}{2} < \theta \leqslant \pi \end{cases}, \tag{10}$$

where a circular beam with a Gaussian distribution of the field strength perpendicular to its optical axis is assumed for the laser irradiation with a spot size of A. Equations (9c–g, k) can be simplified for the case of $F_0(\theta) = 1$, because $I_m = 0$ for $m > 0$, $I_0 = 2$, and $P_0(\cos\theta) = 1$.

However, it is not easy to obtain the thermal conductivity numerically from Eqs. (9) to (10), and the levitated melts observed had an oval shape, not a spherical one. Therefore, numerical simulations that account for deformation of a levitated melt were performed using the commercial software package FIDAP 8.6 [22], which is based on the finite element method. All calculations were carried out with a non-uniform four-node quadrilateral element mesh for the melt as shown in Fig. 2. Equations (2–4) were used in the calculation as the governing equation, the boundary condition, and the initial condition, respectively. A series of phase delays at the equator was calculated as functions of thermal conductivity k and coefficient of heat transfer h_{g0} instead of $h_g(\theta)$ by using FIDAP in advance. The calculation procedure is summarized as the following five steps: (a) the thermal conductivity k was assumed to be a variable parameter from 20 to $100\,\mathrm{W \cdot m^{-1} \cdot K^{-1}}$; (b) the calorific power per unit time and unit volume H in Eq. (2) was determined as a constant value which made the calculated temperature at the equator to be the same value as the measured one under the conditions that the specimen was levitated in vacuum without laser irradiation; (c) constant values Q_0 and Q_1 in Eq. (3) were determined to reproduce the temperature increase and oscillation during irradiation by the CO_2 laser in vacuum; (d) the coefficient of heat transfer h_{g0} was determined to reproduce the temperature decrease during irradiation by the CO_2 laser in gas flow; and (e) the experimental value of the thermal conductivity was determined by a linear interpolation method based on comparison of the phase delay $\Delta\varphi$ obtained experimentally with the calculated one, where $\varepsilon = 0.2$ [23], $C_P = 26\,\mathrm{J \cdot mol^{-1} \cdot K^{-1}}$ at the melting point [6], and the density was substituted by the value determined in the present experiment. A cross-correlation function $C_C(t')$ for the temperature $T(t)$ and the reference signal for controlling the laser power $f(t) \propto Q_0 + Q_1 \sin\omega_0 t$ is as follows:

$$C_C(t') = \frac{\omega_0}{2\pi}\int_0^{2\pi/\omega_0} T(t) f(t - t')\, dt. \tag{11}$$

The phase delay $\Delta\varphi$ was calculated as $\omega_0 t'$ which gave the maximum value of $C_C(t')$.

4. RESULTS AND DISCUSSION

4.1. Density of Silicon Melt

In the vacuum environment on the order of 10^{-2} Pa, a mass decrease of about 50% due to evaporation was measured for the silicon melt one hour after the experiment. Adhesion of silicon powders to the RF coil and vapor deposition of silicon on the view window provided serious problems for temperature measurements of the melt for a long period. In addition, it was not easy to achieve an undercooled state due to nucleation probably caused by adhesion of the powders on the melt surface from the RF coil. On the contrary, the mass decrease was less than 0.1% in an argon–helium mixed atmosphere at atmospheric pressure after the same experimental period. Maximum undercooling of 320 K from the melting point of the silicon melt was achieved independent of the strength of the magnetic field, although the melt motion was damped by applying a magnetic field and contamination from the atmosphere was eliminated by using a high-purity material and cooling gas. Maximum undercooling of a silicon melt was reported as 350 K for an electrostatic levitation method [6], and this value was close to that obtained by the present method. Thus, maximum undercooling of silicon was controlled by the residual impurity in the specimen such as oxides, and not obviously by the melt motion or by contamination of the material.

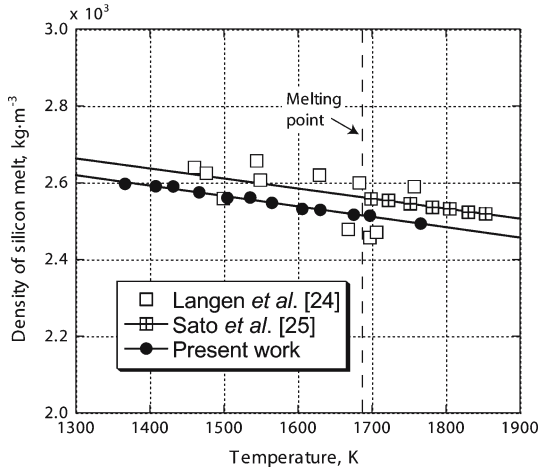

Fig. 4. Temperature dependence of the density of silicon melt.

Figure 4 shows the temperature dependence of the density of a silicon melt obtained by the method. The obtained density for 1367 K $< T <$ 1767 K can be expressed as the following equation by using a least-squares method:

$$\rho\,(T) = 2.51 \times 10^3 - 0.271\,(T - T_{\mathrm{m}})\,\mathrm{kg \cdot m^{-3}}, \tag{12}$$

where $T_{\mathrm{m}} = 1687\,\mathrm{K}$ is the melting point of silicon. The temperature fluctuation of the melt was about $\pm 0.5\,\mathrm{K}$ in the measurement range. The coefficient of thermal expansion β for the melt was obtained using Eq. (12) as the following approximation:

$$\beta = -\frac{1}{\rho\,(T)}\left\{\frac{\mathrm{d}\rho\,(T)}{\mathrm{d}T}\right\} \approx 1.08 \times 10^{-4} + 1.17 \times 10^{-8}\,(T - T_{\mathrm{m}})\,\mathrm{K^{-1}}. \tag{13}$$

The scatter of ρ was less than that obtained by EML without a static magnetic field [24], and the temperature dependence of the density agreed well with that obtained in previous studies [6, 25]. The measurement error of ρ was caused by slight evaporation of the melt, the asymmetry of the melt, the quantization of the edge line, and inhomogeneous distribution of temperature in the melt. The residual axial rotation of the melt makes it possible to maintain axi-symmetry because of the centrifugal force in the melt, as shown in Fig. 2. The maximum radius at the equator of each melt was about 200 pixels on each image, and thus the quantization error of the edge line was at most 2%. The volume deviation due to the asymmetry of the edge line was less than 1%. The temperature gradient in the melt resulting from Joule heating and radiation from the melt surface also causes measurement errors for the melt density, because the present measurement technique is based on isothermal conditions in the melt. If we consider steady-state and spherically symmetric temperature distribution in the melt $T(r)$ with the conditions that H is constant, $h_{\mathrm{g0}} = 0$, and $Q_0 = Q_1 = 0$, temperature difference $T(0) - T(R)$ is obtained from Eqs. (2) and (3) as follows:

$$T\,(0) - T\,(R) = \frac{R}{2k}\varepsilon\sigma_{\mathrm{B}}\left\{T\,(R)^4 - T_{\mathrm{ref}}^4\right\}. \tag{14}$$

The temperature difference can be estimated as 3 K, which corresponds to a measurement error of 0.04%, if we substitute the values $R = 4 \times 10^{-3}\,\mathrm{m}$, $k = 56\,\mathrm{W \cdot m^{-1} \cdot K^{-1}}$ [26], $\varepsilon = 0.2$, $\sigma_{\mathrm{B}} = 5.67 \times 10^{-8}\,\mathrm{W \cdot m^{-2} \cdot K^{-4}}$, $T(R) = 1687\,\mathrm{K}$, and $T_{\mathrm{ref}} = 300\,\mathrm{K}$ for Eq. (13). Therefore, the measurement error of the density was about 3% caused by the quantization error of the edge line and by the asymmetry of the melt.

Although Sasaki et al. [27] reported that the temperature dependence of the density of a silicon melt changes drastically near the melting point, this anomalous behavior was not observed here as shown in Fig. 4. Therefore, the melt structure of silicon showed no obvious change in the temperature range, and the origin of the anomalous increase in the melt density was concluded as oxygen impurities from an SiO_2 crucible in the experiment of Ref. 27. The expansion coefficients calculated by using Eq. (13) were in the range from 1.04×10^{-4} to $1.09 \times 10^{-4}\,\mathrm{K}^{-1}$ for $1367\,\mathrm{K} < T < 1767\,\mathrm{K}$, and the values agreed well with those above the melting point measured by Sato et al. [25]. Therefore, the present results for the density measurements also support a possibility that a silicon melt is a metallic liquid in the temperature range, because the coefficients for most molten melts were calculated as about $1 \times 10^{-4}\,\mathrm{K}^{-1}$ based on the Lucas compilation [25, 28].

4.2. Thermal Conductivity of Silicon Melt

The output signal of the temperature on the melt was slightly distorted by noise from the measurement setup, by weak oscillation of the melt, or by rotation of the melt. The low emissivity of the silicon melt suggests a metal-like property of the melt. Takasuka et al. [23] reported the dominant effect of free electrons on the optical properties of a melt. It is well-known that thermal and electrical conductivities of metals are proportional at a given temperature, but with a decrease in temperature the electrical conductivity increases while the thermal conductivity decreases. This temperature behavior is quantified in the Wiedemann–Franz Law. If the heat transport in a silicon melt is dominated by free electrons, the thermal conductivity is expected to follow the law the same as a metallic melt. Figure 5 shows the temperature dependence of the determined thermal conductivity of the silicon melt accompanied with those values estimated by the Wiedemann–Franz law, $k/\sigma = LT$, where the Lorentz number $L = 2.45 \times 10^{-8}\,\mathrm{W \cdot \Omega \cdot K^{-2}}$, and the electrical conductivity $\sigma = 1.4 \times 10^{6}\Omega^{-1} \cdot \mathrm{m}^{-1}$ [29]. Yamamoto et al. [26] reported that the thermal conductivity at the melting point was $56\,\mathrm{W \cdot m^{-1} \cdot K^{-1}}$, which was almost the same as the value obtained using the Wiedemann–Franz law. In addition, the thermal conductivity determined by the present measurement roughly obeyed the law. Therefore, free electrons in a silicon melt obviously affect the thermal conductivity even in the undercooled state.

The data spread of $\pm 20\%$ for the measured values was mainly due to the following sources: (a) $\pm 5\%$ output power instability of the CO_2 laser irradiation, (b) noise of the temperature output signal, and (c) time fluctuations of the melt motion, the residual internal flow in the

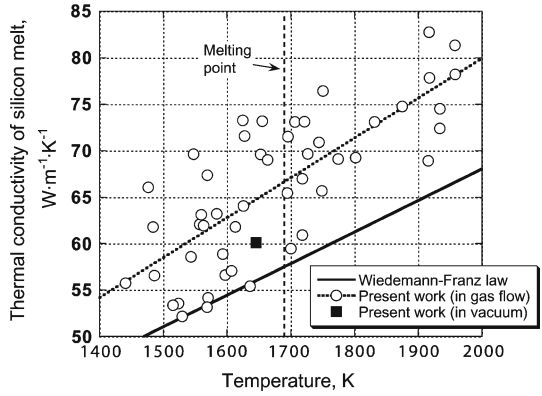

Fig. 5. Temperature dependence of the thermal conductivity of silicon melt.

melt, and $h_g(\theta)$. There are possible reasons for the difference between the measured thermal conductivity from the predicted values using the Wiedemann–Franz law such as (a) difficulty of determining $h_g(\theta)$, (b) convective heat transfer by the residual internal flow, and (c) uncertainty of applying the Wiedemann–Franz law to thermal and electrical conductivities of a semiconductor melt. In vacuum the analysis became simple because of the condition $h_g(\theta) = 0$, whereas it was difficult to widely change the melt temperature by EML without gas flow. On the other hand, large undercooling of the melt was achieved by the gas flow, but it was difficult to determine $h_g(\theta)$ precisely due to the complicated flow field of the gas between the RF coil and the melt. Takasuka et al. [23] reported that the spectral emissivity of silicon melt at 1688 K for the range from 500 to 800 nm was almost 0.27 and the average spectral emissivity from 900 to 2600 nm was 0.21. They also showed that these emissivities had a very weak dependence on temperature from 1688 to 1823 K. Therefore, the present authors presumed that the total hemispherical emissivity was constant and has no temperature dependence even in the undercooled region.

It is still unknown whether or not heat transport in the melt was dominated by thermal diffusion even with the applied magnetic field, because there is no way to measure convection in a metallic melt for EML under a magnetic field at the present moment. The non-axi-symmetric RF coil with a spiral shape generated twisted magnetic lines in the melt, and the rotational component of the melt motion remained even under the magnetic field. The Lorentz force cannot damp the rotation of an axi-symmetric specimen under a homogeneous magnetic field whose direction is parallel to the rotation axis of the specimen z. The real-time observation

with the high-speed camera showed that the rotation rate of the silicon melt from 1 to 6 T was not obviously changed as the value varied between 90 revolutions per second (RPS) and 180 RPS independent of the gas flow. Therefore, the application of an axial magnetic field gradient along the z-axis to a metallic melt is a promising method to damp the rotation, because the Lorentz force in the presence of the radial component of the magnetic field reduces the tangential component of the rotating velocity. It is also necessary for numerical evaluation of the damping effect of a static magnetic field on convection and shape oscillation of the melt to account for the non-axi-symmetric shape of the RF coil. At this point, utilization of a long-duration microgravity environment is still an ideal method to measure the thermal conductivity by using EML more precisely, because a metallic specimen can be stably levitated with a weak RF current. In this case an auxiliary heating apparatus is necessary to raise the sample temperature due to the weak calorific power yielded by the coil, although both the buoyancy force and electromagnetic stirring in the melt are weak. It may be necessary to charge inert gas with low pressure in the chamber, where the condition $h_g(\theta) << 4\varepsilon\sigma T_0^3$ is satisfied, in order to realize the experimental condition that the mass loss is negligible for a long period of the measurement.

5. CONCLUSIONS

Measurements of the density and thermal conductivity of a pure silicon melt over a wide temperature range including the undercooled state were performed by electromagnetic levitation under a magnetic field. The mass loss of the levitated melt was suppressed by controlling the atmosphere in the chamber and thus a maximum undercooling of about 320 K was achieved. The temperature dependence of the determined density showed a linear relation with temperature, and no anomalous increase in the melt density near the melting point was observed. The thermal expansion coefficient agreed well with the value calculated by Sato et al. based on the metallic liquid model. The measured thermal conductivity of the melt agreed roughly with values estimated by the Wiedemann–Franz law, and thus free electrons in a silicon melt obviously affect the thermal conductivity even in the undercooled state.

ACKNOWLEDGMENTS

This research was supported by a Grant-in-Aid for Scientific Research, Scientific Research (A) 15206081 and Scientific Research (B) 16360320 from the Ministry of Education, Culture, Sports, Science, and Technology.

REFERENCES

1. A. F. Norman, K. Eckler, A. Zambon, F. Gatner, S. A. Moir, E. Ramous, D. M. Herlach, and A. L. Greer, *Acta Mater.* **46**:3355 (1998).
2. T. Hibiya and I. Egry, *Meas. Sci. Technol.* **16**:317 (2005).
3. K. Nagashio, Y. Takamura, K. Kuribayashi, and Y. Shiohara, *J. Cryst. Growth* **200**:118 (1999).
4. E. Beagnon and R. Tournier, *Nature* **349**:470 (1991).
5. N. I. Wakayama, M. Ataka, and H. Abe, *J. Cryst. Growth* **178**:653 (1997).
6. W. K. Rhim and K. Osaka, *J. Cryst. Growth* **208**:313 (2000).
7. P.-F. Paradis, T. Ishikawa, and S. Yoda, *Microgravity Sci. Technol.* **XVI-I**:94 (2005).
8. I. Egry, *J. Non-Cryst. Solid* **250–252**:63 (1999).
9. R. P. Liu, D. M. Herlach, M. Vandyoussefi, and A. L. Greer, *Metall. Mater. Trans. A* **35A**:607 (2004).
10. Y. Inatomi, M. Kikuchi, R. Nakamura, K. Kuribayashi, and I. Jimbo, *J. Cryst. Growth* **275**:193 (2005).
11. F. Onishi, Y. Inatomi, T. Tanaka, N. Shinozaki, M. Watanabe, A. Fujimoto, and K. Itoh, *Jpn. J. Appl. Phys.* **45**:5274 (2006).
12. D. T. J. Hurle, E. Jakeman, and C. P. Johnson, *J. Fluid Mech.* **64**:565 (1974).
13. M. Bonvalot, P. Gillon, and R. Tournier, *J. Magn. Magn. Mater.* **151**:283 (1995).
14. P. Gillon, *Mater. Sci. Eng. A* **287**:146 (2000).
15. H. Yasuda, I. Ohnaka, Y. Ninomiya, R. Ishii, and K. Kishio, *Proc. 5th Int. Symp. Magnetic Suspension Technol.* (Turin, 2001), p. 185.
16. I. Ohnaka, Y. Ninomiya, R. Ishii, S. Fujita, and K. Kishio, *J. Cryst. Growth* **260**:475 (2004).
17. T. Miyake, Y. Inatomi, and K. Kuribayashi, *Jpn. J. Appl. Phys.* **41**:L811 (2002).
18. F. Onishi, K. Nagashio, Y. Inatomi, and K. Kuribayashi, *J. Jpn. Soc. Microgravity Appl.* **23**:26 (2006).
19. R. C. Bradshaw, D. P. Schmidt, J. R. Rogers, K. F. Kelton, and R. W. Hyers, *Rev. Sci. Instrum.* **76**:125108 (2005).
20. Y. Shimizu, J. Ishii, K. Shinzato, and T. Baba, *Int. J. Thermophys.* **26**:203 (2005).
21. F. Onishi, K. Nagashio, Y. Inatomi, and K. Kuribayashi, *Jpn. J. Thermophys. Prop.* **25**:186 (2004).
22. M. S. Engelman, *FAIDAP8.0* (Fluent Inc., Lebanon, New Hampshire, 1998).
23. E. Takasuka, E. Tokizaki, K. Terashima, and S. Kimura, *Jpn. J. Appl. Phys.* **81**:6384 (1997).
24. M. Langen, T. Hibiya, M. Eguchi, and I. Egry, *J. Cryst. Growth* **186**:550 (1998).
25. Y. Sato, T. Nishizuka, K. Hara, T. Yamamura, and Y. Waseda, *Int. J. Thermophys.* **21**:1463 (2000).
26. H. Sasaki, A. Ikari, K. Terashima, and S. Kimura, *Jpn. J. Appl. Phys.* **34**:3426 (1995).
27. H. Sasaki, E. Tokizaki, K. Terashima, and S. Kimura, *Jpn. J. Appl. Phys.* **33**:6078 (1994).
28. L. D. Lucas, *Techniques of Metals Research*, Vol. IV, Part 2 (John Wiley, New York, 1970), pp. 219-292.
29. K. Yamamoto, T. Abe, and S. Takasu, *Jpn. J. Appl. Phys.* **30**:2423 (1991).